Electrodeposition

International Edition: DOI: 10.1002/anie.201509364
German Edition: DOI: 10.1002/ange.201509364

Dendrite-Free Nanocrystalline Zinc Electrodeposition from an Ionic Liquid Containing Nickel Triflate for Rechargeable Zn-Based Batteries

*Zhen Liu, Tong Cui, Giridhar Pulletikurthi, Abhishek Lahiri, Timo Carstens, Mark Olschewski, and Frank Endres**

Abstract: *Metallic zinc is a promising anode material for rechargeable Zn-based batteries. However, the dendritic growth of zinc has prevented practical applications. Herein it is demonstrated that dendrite-free zinc deposits with a nanocrystalline structure can be obtained by using nickel triflate as an additive in a zinc triflate containing ionic liquid. The formation of a thin layer of Zn–Ni alloy (η- and γ-phases) on the surface and in the initial stages of deposition along with the formation of an interfacial layer on the electrode strongly affect the nucleation and growth of zinc. A well-defined and uniform nanocrystalline zinc deposit with particle sizes of about 25 nm was obtained in the presence of Ni^{II}. Further, it is shown that the nanocrystalline Zn exhibits a high cycling stability even after 50 deposition/stripping cycles. This strategy of introducing an inorganic metal salt in ionic liquid electrolytes can be considered as an efficient way to obtain dendrite-free zinc.*

Rechargeable zinc-based batteries, especially Zn–air batteries, have great potential for next-generation energy storage devices owing to their low cost, inflammability, low toxicity, and promising energy density.[1] However, the development of rechargeable Zn-based batteries has been hindered mainly by the formation of Zn dendrites during charging, leading to a capacity fading or even short circuiting of the cell.[2] Many approaches have been proposed to suppress dendritic Zn growth by adding additives to the electrolyte,[3] alloying the Zn anode with other metals,[4] and modifying the Zn anode with organic or inorganic materials.[5] Although these strategies are promising, the battery still suffers reduced anode capacity, low Coulombic efficiency, short cycle life, and safety issues in aqueous and/or organic electrolytes.[6] Ionic liquids (ILs) exhibit good electrical conductivity, high thermal stability, and large electrochemical windows and are promising electrolytes for batteries.[7] The electrodeposition of zinc from ionic liquids has already been demonstrated[8] and the morphology of Zn deposits is strongly dependent on the structure of the ILs probably as a result of variations in the interfacial behavior of ILs.[9]

The deposition of Zn from $Zn(TfO)_2$ in 1-butyl-1-methylpyrrolidinium trifluoromethylsulfonate ($[Py_{1,4}]TfO$) leads to nanocrystalline deposits, whereas in 1-ethyl-3-methylimidazolium trifluoromethylsulfonate ([EMIm]TfO) a microcrystalline deposit is obtained.[8a] However, dendritic growth of Zn is still inevitable in ILs,[10] especially at elevated temperatures.[8a] The addition of additives to ILs is a relatively new approach and some studies have been performed in order to obtain dendrite-free metal deposits in ILs, including the addition of organic compounds to suppress Zn dendrites,[11] alkali and alkaline-earth metal salts to suppress lithium dendrites,[12] and $SiCl_4$ in MCl_n/IL (M = Sn, Zn, and Te; $n = 2$, 4) to obtain metal nanowires.[13] Furthermore, the formation of a solid electrolyte interface (SEI) on the electrode surfaces has also been reported to be an efficient way to prevent dendrite growth of metals, especially in suppressing lithium dendritic growth.[14]

Herein, we report for the first time the addition of $Ni(TfO)_2$ to $Zn(TfO)_2$ in [EMIm]TfO to obtain dendrite-free Zn deposits with a nanocrystalline structure, and demonstrate their cycling performance.

Figure 1a shows the cyclic voltammograms of 0.1 M $Zn(TfO)_2$ in [EMIm]TfO on gold in the presence and absence of 0.015 M $Ni(TfO)_2$. In the absence of Ni^{II}, the deposition of zinc starts at a potential of around −1.55 V during the cathodic scan. In the anodic regime, a maximum current density of 4 mA cm^{-2} was recorded at −0.87 V followed by a sharp decrease in the current to zero. In the presence of Ni^{II}, a potential of −1.65 V is required for the nucleation of zinc. In the anodic regime, the stripping peak significantly shifts to more positive potentials and the peak becomes broader, which might be due to the oxidation of Zn and Zn–Ni alloys. The CVs retain their shapes even after 10 cycles, indicating a reversible Zn deposition/stripping process (Figure S1 in the Supporting Information).

In the inset of Figure 1a, the CV of 0.015 M $Ni(TfO)_2$ in [EMIm]TfO shows a reduction peak (c*) at −2.2 V prior to the reduction of the $[EMIm]^+$ cation. Electrolysis at −2.2 V for 2 h did not produce any nickel on the surface as investigated by XPS. Similar electrochemical behavior was also reported by Gou et al. for nickel chloride/zinc chloride in 1-ethyl-3-methylimidazolium chloride.[15] Further investigations, like in situ scanning tunneling microscopy (STM), may provide more information on this process.

On potentiostatic electrolysis of 0.015 M $Ni(TfO)_2$ in [EMIm]TfO at 100 °C and −1.2 V for 2 h, a black layer was obtained. The deposits exhibit spherical nanocrystals and energy-dispersive X-ray spectroscopy (EDX) shows a large amount of sulfur with a Ni/S molar ratio of 2:1 (Figure S2a,b). XRD results (Figure S2c) indicated that the deposit contains metallic nickel and Ni_3S_2. We further carried out X-ray

[*] Dr. Z. Liu, T. Cui, Dr. G. Pulletikurthi, Dr. A. Lahiri, Dr. T. Carstens, M. Olschewski, Prof. Dr. F. Endres
Institute of Electrochemistry
Clausthal University of Technology
Arnold-Sommerfeld-Strasse 6,Clausthal-Zellerfeld, 38678 (Germany)
E-mail: frank.endres@tu-clausthal.de

Supporting information for this article is available on the WWW under http://dx.doi.org/10.1002/anie.201509364.

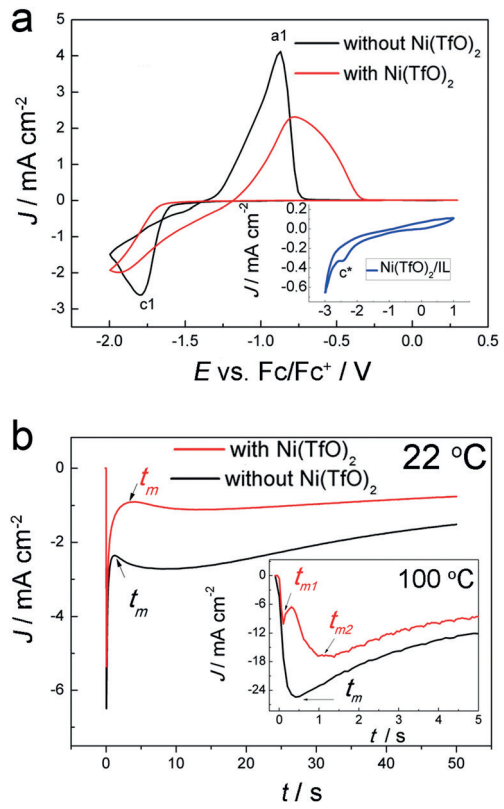

Figure 1. a) CVs of 0.1 M $Zn(TfO)_2$ in [EMIm]TfO without and with 0.015 M $Ni(TfO)_2$ on gold at 22 °C; inset shows the CV of 0.015 M $Ni(TfO)_2$ in [EMIm]TfO on gold. Scan rate: 10 mV s^{-1}. b) Chronoamperograms of 0.1 M $Zn(TfO)_2$ in [EMIm]TfO without and with 0.015 M $Ni(TfO)_2$ on gold at 22 °C and at 100 °C (inset).

photoelectron spectroscopy (XPS) to characterize the chemical compositions of the deposit. Figure S2 d–f shows the survey curves, Ni2p and S2p, including peak deconvolution and assignments of the deposits. The results indicated that $NiSO_4$, $NiSO_3$, Ni_xS_y, and metallic Ni were formed on the electrode. It was reported that the reductive decomposition of bis(trifluoromethylsulfonyl)amide (TFSA) anions occurs during cathodic polarization.[16] The TfO anions are less electrostable than TFSA anions.[17] Therefore, the TfO anion is also expected to decompose under cathodic polarization. The resulting decomposed species can interact with Ni^{2+} which was shown to form a solid electrolyte interphase (SEI layer) on the surface. Such a SEI layer was not observed in 0.1 M $Zn(TfO)_2$ in [EMIm]TfO. The solubility of $Zn(TfO)_2$ in [EMIm]TfO (> 0.6 M) at 22 °C is 20 times higher than that of $Ni(TfO)_2$ in [EMIm]TfO (ca. 0.03 M). Therefore, nickel salts will precipitate more easily.

In the chronoamperometric profiles (Figure 1 b) recorded upon applying potential (−1.7 V) the current–time transients are characterized by a rising current due to formation and growth of nuclei on the substrate until a current maximum (i_m) is attained at a time maximum (t_m) followed by Cottrell behavior. In the presence of Ni^{II}, the chronoamperogram shows a decrease in the current and i_m is attained at longer t_m. This suggests that the nucleation and growth of zinc is distinctly changed in the presence of Ni^{II}. The transient exhibits a more complicated form involving two growth processes in the presence of Ni^{II} at 100 °C and −1.2 V as shown in the inset of Figure 1 b. The first process (t_{m1}), which occurs at shorter time than that in the absence of Ni^{II} (t_m), might be related to the co-deposition of Zn–Ni alloy and/or the formation of a SEI layer on the gold surface. The second process (t_{m2}), which occurs at a longer time and with a lower current than that in the absence of Ni^{II} (t_m), probably is a result of the deposition of zinc in presence of a SEI layer.

To further evaluate the electrochemical processes, in situ atomic force microscopy (AFM) was performed. Force–distance curves from AFM studies have revealed that the interfacial layer in ionic liquids has a multilayered arrangement at the electrode/electrolyte interface.[18] The interfacial structure can be divided into three regions: the innermost layer, the transition zone, and the bulk liquid.[19] The innermost layer of ionic species is in direct contact with the electrode surface and shows the highest order. Therefore, in situ AFM studies were performed on [EMIm]TfO, $Zn(TfO)_2$ in [EMIm]TfO, and $Zn(TfO)_2$ and $Ni(TfO)_2$ in [EMIm]TfO as a function of potential on Au(111). Four discrete steps in the force–distance curve were observed in pure [EMIm]TfO at −0.2 V (Figure 2 a). The force required to rupture the innermost layer is 5 nN with a width of the innermost layer of 0.68 nm, which corresponds to the presence of an IL ion pair. The [EMIm]TfO ion pair has an estimated diameter of 0.68 nm when one assumes a cubic packing geometry.[20] The addition of a metal salt significantly changes the IL interface.[21] Upon the addition of 0.1 M $Zn(TfO)_2$, the width of the innermost layer is lowered to 0.48 nm, probably as a result of the replacement of $[EMIm]^+$ with Zn^{2+} complexes. When 0.015 M $Ni(TfO)_2$ is present, the width of the innermost layer further decreases to 0.27 nm. It appears that in the presence of two cations, Ni^{2+} and Zn^{2+}, the interfacial structure is significantly altered. When the potential is changed to −0.5 V (Figure 2 b), the innermost layer shows a decreased distance of 0.62 nm in [EMIm]TfO probably as IL ion pairs adopt an orientation more parallel to the surface,[22] whereas the separation distance remains unchanged in the presence of the metal salts. When the potential is changed further to −0.8 V, the force required to rupture the innermost layer is 11 nN in the presence of Ni^{II}, which is three times larger than that in the absence of Ni^{II} (Figure 2 c), indicating stronger interfacial electrostatic interactions with gold. The separation distance also slightly increases to 0.31 nm. The second and third layers have a separation of 0.65 nm in the presence of Ni^{II}, which indicates the presence of IL ion pairs. Thus, the AFM results clearly indicate that the addition of metal salts significantly alters the interfacial structure at the electrode/electrolyte interface which in turn might affect the electrochemical process as evidenced by the CVs in Figure 1.

Scanning electron microscopy (SEM) images of the deposited Zn films are shown in Figure 3. In the absence of Ni^{II}, aggregates of hexagonal plate-like Zn crystals were obtained (Figure 3 a and Figure S3 a with low magnification). The cross-sectional view shows fibrous-like growth (Figure 3 b). When the concentration of $Zn(TfO)_2$ was increased to 0.2 M, dendritic growth of Zn was observed.[10] However, in the presence of Ni^{II}, uniform and well-defined Zn nano-

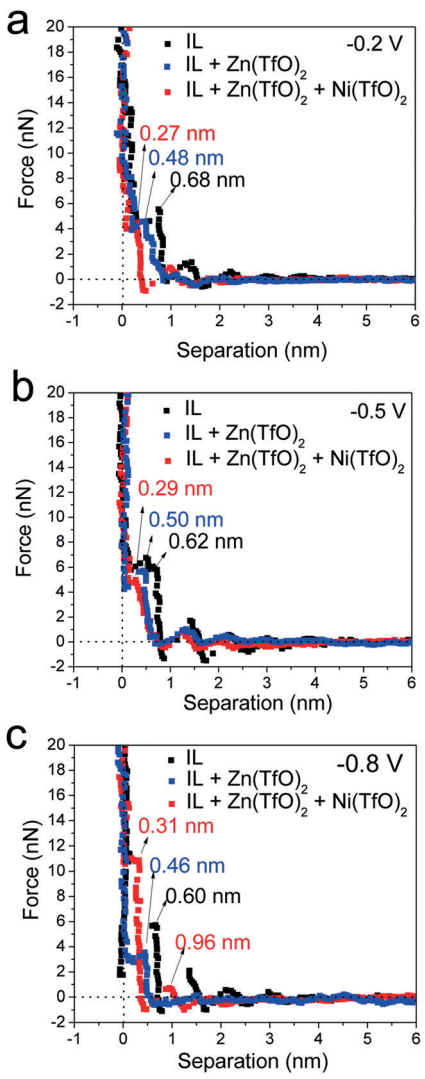

Figure 2. Force versus apparent separation profiles for a silica cantilever approaching an Au(111) surface in [EMIm]TfO, 0.1 M $Zn(TfO)_2$ in [EMIm]TfO, and 0.1 M $Zn(TfO)_2$ and 0.015 M $Ni(TfO)_2$ in [EMIm]TfO, respectively, at a) −0.2 V, b) −0.5 V, and c) −0.8 V.

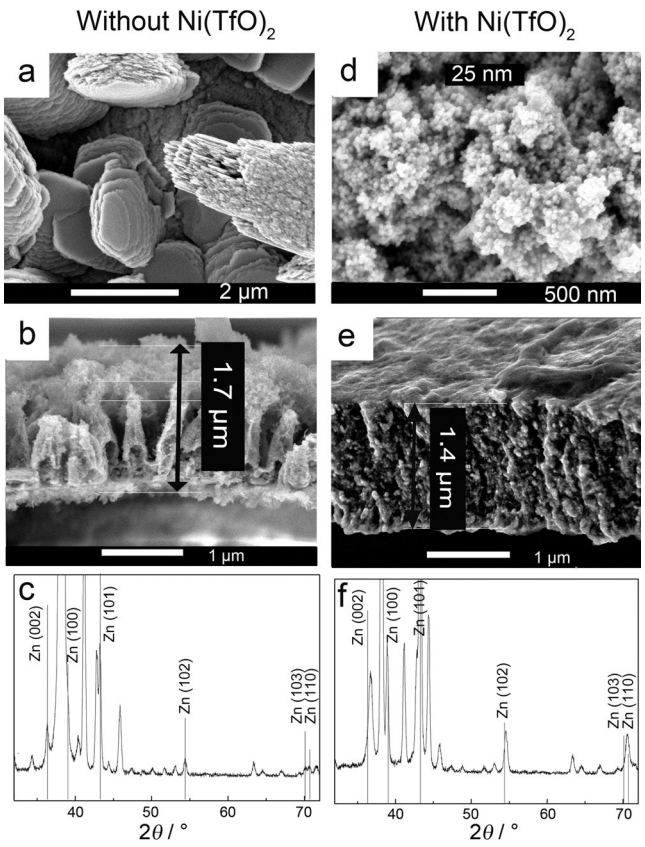

Figure 3. Morphologies (a,b,d,e) and XRD (c,f) of Zn films on gold obtained from 0.1 M $Zn(TfO)_2$ in [EMIm]TfO (a–c) and with 0.015 M $Ni(TfO)_2$ (d–f) at −1.7 V for 2 h.

crystalline structures with particle sizes of about 25 nm were obtained (Figure 3d and Figure S3b with low magnification). From the cross-sectional view (Figure 3e) it is evident that the deposits are dense and compact. Visually, the deposit has a black appearance in the presence of Ni^{II}, whereas a silver-gray zinc deposit is observed in the absence of Ni^{II} (Figure S4). EDX results (Figure S3b) show that the deposit has a Zn/Ni molar ratio of 48:2. At low Ni contents (< 15 atom %), Zn–Ni alloys exhibit mainly η-phase and γ-phase. The η-phase has a hexagonal crystal structure with a Ni content of less than 1%. The γ-phase has a body-centered cubic structure with the composition of Ni_5Zn_{21} (8–15% Ni).[23]

The X-ray diffraction (XRD) pattern of Zn obtained from 0.1M $Zn(TfO)_2$ in [EMIm]TfO (Figure 3c) shows peaks at (002), (100), (101), (102), (103), and (110), matching well with the Zn reference (JCPDS No: 04-0831). However, in the presence of Ni^{II}, the major peaks of the Zn deposit at the (100) and (101) planes were not shifted from their equilibrium positions. The less intense peaks related to (002), (102), (103), and (110) planes were shifted to higher angles indicating reduced d-spacings (Figure 3f). The peak shift can be due to changes in the chemical composition. The incorporation of Ni in the Zn lattice causes a cell distortion but the unit still remains hexagonal, and thus the diffraction lines shift their positions.[24] Therefore, these peaks might be from the η-phase of a Zn–Ni alloy. An additional peak at 42.8° was also observed, which is related to the (411) plane of Ni_5Zn_{21} (γ-phase; JCPDS No.: 06-0653) (Figure S5). We also investigated the XPS of the sample (Figure S6), and no Ni was found on the surface even it had been etched with Ar^+ for 20 min. This suggests that the Zn–Ni alloys are formed only at the initial stages of deposition and then the growth of Zn takes place.

In order to shed more light on the deposition process in the presence of Ni^{II}, electrolysis was performed to study the effect of potential, temperature, and morphology changes on different substrates. The morphologies of the Zn deposits obtained at different potentials (−1.6, −1.8, and −2.0 V) on gold at 22 °C are shown in Figure S7. At all the investigated potentials, uniform dendrite-free Zn deposits with particle sizes ranging from 20 to 30 nm were obtained. When the temperature was increased to 100 °C, a relatively rough surface with Zn particle sizes of about several hundred nanometers was obtained. A microcrystalline Zn deposit with

particle sizes of roughly 5 μm was obtained in the absence of Ni^{II} (Figures S8 and S9). EDX results reveal (Figure S8) that the Zn/Ni molar ratio is 40:1 and XPS (Figure S10) shows still no Ni on the surface. We also investigated the Zn deposition on copper and the results show that nanocrystalline Zn is formed in a similar manner to that of gold, irrespective of the substrate (Figure S11).

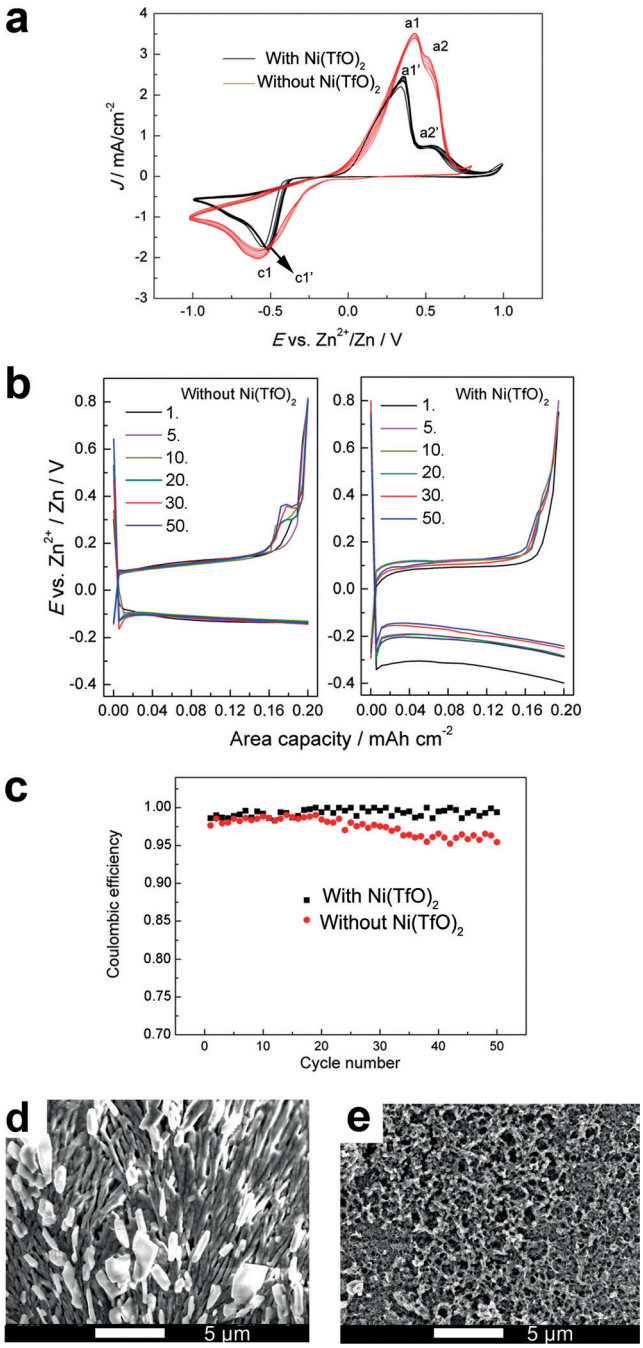

Figure 4. a) CVs of 0.1 M $Zn(TfO)_2$ in [EMIm]TfO without and with 0.015 M $Ni(TfO)_2$ cycled on Cu; scan rate: 10 $mV s^{-1}$. b) Voltage profiles of the Zn deposition/dissolution process at a current density of 0.2 $mA cm^{-2}$. c) Coulombic efficiency vs. cycle number and morphology of Zn deposits at the edge of the electrode after 50 cycles without Ni^{II} (d) and with (e) 0.015 M $Ni(TfO)_2$.

In rechargeable Zn-based batteries, the cycling performance of the Zn anode is critical for the battery life. CV results show an increased overpotential for the deposition of zinc in the presence of $Ni(TfO)_2$ (Figure 4a). In the anodic regime, two oxidation processes were observed in both cases. The first peak a1 or a1′ is attributed to the oxidation of Zn and the second peak a2 or a2′ can be due to the oxidation of the Cu–Zn alloy. The voltage differences between the peaks is roughly 0.1 V in the absence of Ni^{II} and about 0.2 V in the presence of Ni^{II}. This indicates that the stripping of Zn is more likely accompanied by the stripping of Zn–Cu alloy in the absence of Ni^{II}. Figure 4b shows voltage profiles of different cycles. A stable overpotential of ca. 0.1 V was recorded during charging in the absence of Ni^{II}, whereas an overpotential of −0.35 V is required in the initial cycles and roughly −0.20 V in the following cycles (5th to 50th) in the presence of Ni^{II}, indicating the formation of a SEI layer. During discharging, the electrode exhibits two distinguishable potential plateaus (0.1 and 0.3 V) in the absence of Ni^{II}, whereas only one obvious plateau was observed in the presence of Ni^{II}. At a discharge capacity of 0.2 $mAh cm^{-2}$, the cell maintains an average Coulombic efficiency of more than 99% after 50 cycles in the presence of Ni^{II}, whereas in the absence of Ni^{II} the efficiency decreases to 95% after just 25 cycles (average Coulombic efficiency over the first 25 cycles is 99%) (Figure 4c). These results clearly demonstrate that the presence of $Ni(TfO)_2$ in the electrolyte increases the stability of the Zn anode. The morphology of the Zn deposits after 50 cycles shows a behavior that is characteristic of dendritic formation in the absence of Ni^{II} (Figure 4d), whereas a dendrite-free Zn structure with a high porosity was observed in the presence of Ni^{II} (Figure 4e).

In summary, we have shown that dendrite-free Zn with a nanocrystalline structure can be obtained from $Zn(TfO)_2$ in [EMIm]TfO in the presence of $Ni(TfO)_2$. The addition of metal salts to ionic liquids appears to have altered the interfacial layer structure. A thin film of Zn–Ni alloy formed on the surface together with the formation of a SEI layer affects the nucleation and growth of Zn. Furthermore, the nanostructured Zn electrode shows remarkable electrochemical performance and structural stability, leading to a cycle life suitable for rechargeable Zn-based batteries. This work presents a simple and effective strategy to inhibit dendritic growth of Zn and may open up new possibilities for applications in new energy storage systems.

Acknowledgements

Financial support by the BMBF project LUZI (BMBF: 03SF0499A) is gratefully acknowledged.

Keywords: dendrite-free deposition · electrochemistry · ionic liquids · nickel · zinc

How to cite: *Angew. Chem. Int. Ed.* **2016**, *55*, 2889–2893
Angew. Chem. **2016**, *128*, 2939–2943

[1] a) Y. Li, H. Dai, *Chem. Soc. Rev.* **2014**, *43*, 5257 – 5275; b) J. F. Parker, C. N. Chervin, E. S. Nelson, D. R. Rolison, J. W. Long, *Energy Environ. Sci.* **2014**, *7*, 1117 – 1124.

[2] a) Y. Shen, K. Kordesch, *J. Power Sources* **2000**, *87*, 162 – 166; b) Y. Ito, M. Nyce, R. Plivelich, M. Klein, D. Steingart, S. Banerjee, *J. Power Sources* **2011**, *196*, 2340 – 2345.

[3] a) S. J. Banik, R. Akolkar, *J. Electrochem. Soc.* **2013**, *160*, D519 – D523; b) M. Xu, D. G. Ivey, W. Qu, Z. Xie, *J. Power Sources* **2015**, *274*, 1249 – 1253; c) O. Aaboubi, J. Douglade, X. Abenaqui, R. Boumedmed, J. VonHoff, *Electrochim. Acta* **2011**, *56*, 7885 – 7889; d) S. J. Banik, R. Akolkar, *Electrochim. Acta* **2015**, *179*, 475 – 481.

[4] C. W. Lee, K. Sathiyanarayanan, S. W. Eom, M. S. Yun, *J. Power Sources* **2006**, *160*, 1436 – 1441.

[5] a) J. F. Parker, E. S. Nelson, M. D. Wattendorf, C. N. Chervin, J. W. Long, D. R. Rolison, *ACS Appl. Mater. Interfaces* **2014**, *6*, 19471 – 19476; b) S.-M. Lee, Y.-J. Kim, S.-W. Eom, N.-S. Choi, K.-W. Kim, S.-B. Cho, *J. Power Sources* **2013**, *227*, 177 – 184; c) H. Li, C. Xu, C. Han, Y. Chen, C. Wei, B. Li, F. Kang, *J. Electrochem. Soc.* **2015**, *162*, A1439 – A1444.

[6] P. Pei, K. Wang, Z. Ma, *Appl. Energy* **2014**, *128*, 315 – 324.

[7] a) F. Endres, S. Zein El Abedin, *Phys. Chem. Chem. Phys.* **2006**, *8*, 2101 – 2116; b) M. Armand, F. Endres, D. R. MacFarlane, H. Ohno, B. Scrosati, *Nat. Mater.* **2009**, *8*, 621 – 629; c) A. P. Abbott, K. J. McKenzie, *Phys. Chem. Chem. Phys.* **2006**, *8*, 4265 – 4279.

[8] a) Z. Liu, S. Zein El Abedin, F. Endres, *Electrochim. Acta* **2013**, *89*, 635 – 643; b) T. J. Simons, A. A. J. Torriero, P. C. Howlett, D. R. MacFarlane, M. Forsyth, *Electrochem. Commun.* **2012**, *18*, 119 – 122; c) A. P. Abbott, J. C. Barron, K. S. Ryder, *Trans. Inst. Met. Finish.* **2009**, *87*, 201 – 207.

[9] F. Endres, O. Hofft, N. Borisenko, L. H. Gasparotto, A. Prowald, R. Al-Salman, T. Carstens, R. Atkin, A. Bund, S. Zein El Abedin, *Phys. Chem. Chem. Phys.* **2010**, *12*, 1724 – 1732.

[10] Z. Liu, S. Zein El Abedin, M. S. Ghazvini, F. Endres, *Phys. Chem. Chem. Phys.* **2013**, *15*, 11362 – 11367.

[11] a) A. P. Abbott, J. C. Barron, G. Frisch, K. S. Ryder, A. F. Silva, *Electrochim. Acta* **2011**, *56*, 5272 – 5279; b) Z. Liu, S. Zein El Abedin, N. Borisenko, F. Endres, *ChemElectroChem* **2015**, *2*, 1159 – 1163; c) N. M. Pereira, P. M. V. Fernandes, C. M. Pereira, A. F. Silva, *J. Electrochem. Soc.* **2012**, *159*, D501 – D506.

[12] a) J. K. S. Goodman, P. A. Kohl, *J. Electrochem. Soc.* **2014**, *161*, D418 – D424; b) J. K. Stark, Y. Ding, P. A. Kohl, *J. Electrochem. Soc.* **2013**, *160*, D337 – D342; c) J. K. Stark, Y. Ding, P. A. Kohl, *J. Electrochem. Soc.* **2011**, *158*, A1100 – A1105.

[13] a) R. Al-Salman, H. Sommer, T. Brezesinski, J. Janek, *Chem. Mater.* **2015**, *27*, 3830 – 3837; b) A. M. Elbasiony, M. Olschewski, S. Zein El Abedin, F. Endres, *ChemElectroChem* **2015**, *2*, 1361 – 1365.

[14] a) W. Li, H. Yao, K. Yan, G. Zheng, Z. Liang, Y.-M. Chiang, Y. Cui, *Nat. Commun.* **2015**, *6*, 7436; b) W. Xu, J. Wang, F. Ding, X. Chen, E. Nasybulin, Y. Zhang, J.-G. Zhang, *Energy Environ. Sci.* **2014**, *7*, 513 – 537; c) S. S. Zhang, *J. Power Sources* **2006**, *162*, 1379 – 1394; d) E. Peled, *J. Electrochem. Soc.* **1979**, *126*, 2047 – 2051.

[15] S.-P. Gou, I. W. Sun, *Electrochim. Acta* **2008**, *53*, 2538 – 2544.

[16] a) E. Markevich, R. Sharabi, V. Borgel, H. Gottlieb, G. Salitra, D. Aurbach, G. Semrau, M. A. Schmidt, *Electrochim. Acta* **2010**, *55*, 2687 – 2696; b) P. C. Howlett, E. I. Izgorodina, M. Forsyth, D. R. MacFarlane, *Z. Phys. Chem. (Muenchen Ger.)* **2006**, *220*, 1483 – 1498.

[17] M. Hayyan, F. S. Mjalli, M. A. Hashim, I. M. AlNashef, T. X. Mei, *J. Ind. Eng. Chem.* **2013**, *19*, 106 – 112.

[18] a) R. Atkin, M. Drüschler, S. Zein El Abedin, F. Endres, B. Huber, B. Roling, *Phys. Chem. Chem. Phys.* **2011**, *13*, 6849 – 6857; b) R. Atkin, G. G. Warr, *J. Phys. Chem. C* **2007**, *111*, 5162 – 5168; c) R. Hayes, S. Zein El Abedin, R. Atkin, *J. Phys. Chem. B* **2009**, *113*, 7049 – 7052; d) R. Hayes, G. G. Warr, R. Atkin, *Phys. Chem. Chem. Phys.* **2010**, *12*, 1709 – 1723; e) R. Hayes, N. Borisenko, M. K. Tam, P. C. Howlett, F. Endres, R. Atkin, *J. Phys. Chem. C* **2011**, *115*, 6855 – 6863.

[19] "Interfaces of Ionic Liquids (2)": R. Hayes, D. Wakeham, R. Atkin, in *Ionic Liquids UnCOILed*, Wiley, New York, **2012**, pp. 51 – 85.

[20] H. Li, F. Endres, R. Atkin, *Phys. Chem. Chem. Phys.* **2013**, *15*, 14624 – 14633.

[21] a) A. Lahiri, T. Carstens, R. Atkin, N. Borisenko, F. Endres, *J. Phys. Chem. C* **2015**, *119*, 16734 – 16742; b) F. Endres, S. Zein El Abedin, N. Borissenko, *Z. Phys. Chem. (Muenchen Ger.)* **2006**, *220*, 1377 – 1394; c) R. Hayes, N. Borisenko, B. Corr, G. B. Webber, F. Endres, R. Atkin, *Chem. Commun.* **2012**, *48*, 10246 – 10248.

[22] S. Baldelli, *Acc. Chem. Res.* **2008**, *41*, 421 – 431.

[23] S. Swathirajan, *J. Electrochem. Soc.* **1986**, *133*, 671 – 680.

[24] B. D. Cullity, *Elements of X-ray Diffraction*, 2nd ed., Addison-Wesley, Reading, MA, **1978**, pp. 314 – 316.

Received: October 7, 2015
Published online: January 28, 2016

